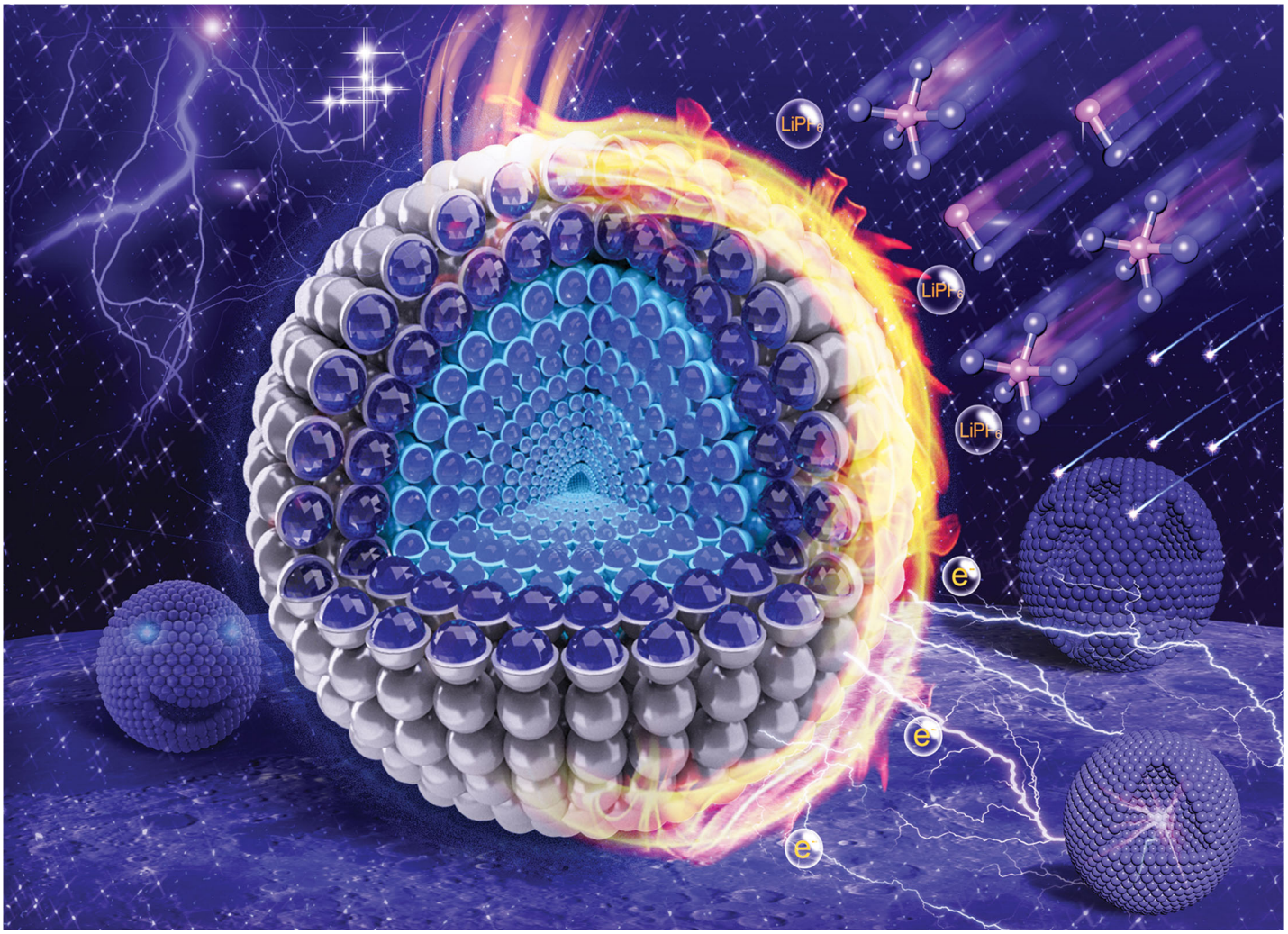

Showcasing research from Professor Weidong He's laboratory, School of Physics, University of Electronic Science and Technology of China, Chengdu, China.

Origin of extra capacity in the solid electrolyte interphase near high-capacity iron carbide anodes for Li ion batteries

A core-shell Fe_3C nanostructure anode is designed to investigate the origin of its extra capacity. By revealing the structural and physiochemical evolution of the SEI, both organic and inorganic ingredients undergo reversible conversions and contribute capacity enhancement to the catalysis of Fe_3C. This process is enhanced through the decreased d-band center of C@Fe_3C due to the robust host–guest electronic interaction between encased Fe_3C and protective graphitic layers. This study provides a novel scheme for efficiently utilizing catalysis-based anodes to realize next-generation lithium ion batteries.

As featured in:

See Weidong He *et al.*, *Energy Environ. Sci.*, 2020, **13**, 2924.

ROYAL SOCIETY OF CHEMISTRY

rsc.li/ees

Registered charity number: 207890

Energy & Environmental Science

ROYAL SOCIETY OF CHEMISTRY

PAPER

View Article Online
View Journal | View Issue

Cite this: *Energy Environ. Sci.*, 2020, **13**, 2924

Origin of extra capacity in the solid electrolyte interphase near high-capacity iron carbide anodes for Li ion batteries†

Dongjiang Chen,[a] Chao Feng,[a] Yupei Han,[a] Bo Yu,[a] Wei Chen,[a] Ziqi Zhou,[a] Ning Chen,[a] John B. Goodenough[b] and Weidong He*[ac]

Received 17th December 2019,
Accepted 14th May 2020

DOI: 10.1039/c9ee04062e

rsc.li/ees

Transition metal carbides (TMCs), known to deliver extra capacity beyond the theoretical limit, are proposed as emerging high-capacity anodes for next-generation lithium ion batteries (LIBs). Nevertheless, the underlying mechanism for the extra lithium storage in TMCs has not been revealed clearly due to the electrochemical inertness of TMCs to Li in cycling. Here, for the first time, by employing *in situ* Raman and X-ray photoelectron spectroscopies, we corroborate that the capacity enhancement of Fe_3C anodes originates from the physiochemical evolution of solid electrolyte interphase (SEI) and surface carbonaceous materials through three mechanisms: (i) Fe_3C catalyzes the reversible conversion between esters and ethers to store extra lithium ions in the SEI; (ii) Fe and inorganic components embedded in the SEI form a reversible surface-conversion reaction of $Fe + 3LiF \rightleftharpoons FeF_3 + 3Li^+ + 3e^-$ to contribute additional capacity; and (iii) surficial carbon delivers capacity through surface capacitive effects and Li^+ inter/deintercalation processes. With the extra lithium ion storage in the SEI and carbon, the C@Fe_3C/Fe anode delivers a high reversible capacity of 808 mA h g^{-1} after 700 cycles at 1 A g^{-1}. This study provides a fundamental basis for emerging high-capacity TMC anodes to be efficiently explored for next-generation LIBs.

Broader context

There is intensive interest in developing high-capacity and long-life lithium-ion batteries for applications in electric vehicles, electronic devices and large-scale power sources. Underlying these initiatives are strategies for designing upgraded electrode materials. Fe_3C, an anode that delivers extra capacity beyond the theoretical limit, is arguably a promising candidate for next-generation energy conversion and storage applications due to its high electrical conductivity ($\sim 10^6$ S m^{-1}), electrochemical stability and excellent rate capabilities. However, the prebiotic chemistry regarding the capacity enhancement of transition-metal carbide anodes still remains poorly understood due to their electrochemical inertness to Li in cycling. Herein, by revealing the structural and physiochemical evolution of the solid electrolyte interphase (SEI) near a core–shell C@Fe_3C/Fe anode in pre-designed electrolytes with various fluorine contents, we corroborate that both organic and inorganic ingredients of SEI undergo reversible conversions and contribute capacity enhancement through the catalysis of Fe_3C. The surface capacitive effect and Li^+ inter/deintercalation processes of carbonaceous materials are revealed to be non-negligible for the additional capacity. The findings offer fundamental insights into high-capacity catalysis-based anodes to realize safe, high-capacity next-generation energy storage devices.

Introduction

Lithium ion batteries (LIBs) have found extensive applications in a variety of applications, such as portable electronics, electric vehicles, solar/wind energy storage, and implantable medical devices, owing to the zero memory effect, reliable security, and long lifetime.[1–8] High-capacity electrode materials are the key to developing high-energy-density LIBs. To date, the intercalation-type graphite anode still prevails in the applications of LIBs, while its relatively low theoretical capacity (372 mA h g^{-1}), unqualified electronic conductivity ($\sim 10^5$ S m^{-1}) and inferior rate performances fail to meet the growing demands of LIBs.[9–12]

Fe_3C, a classical transition metal carbide (TMC), has been proposed as a potential next-generation anode material due to its high electrical conductivity ($\sim 10^6$ S m^{-1}), electrochemical stability and excellent rate capability.[13–15] In addition, its extreme

[a] School of Physics, University of Electronic Science and Technology of China, Chengdu 611731, China. E-mail: weidong.he@uestc.edu.cn
[b] Materials Science and Engineering Program & Texas Materials Institute, The University of Texas at Austin, Austin, TX 78712, USA
[c] National Key Laboratory of Science and Technology on Advanced Composites in Special Environments, and Center for Composite Materials and Structures, Harbin Institute of Technology, Harbin 150080, China

† Electronic supplementary information (ESI) available. See DOI: 10.1039/c9ee04062e

hardness and thermal stability enable safe LIB operation under extreme conditions. In the Fe_3C crystal, carbon atoms occupy the interstitial sites of close-packed Fe atoms, where the contracted d-band electrons near the Fermi level contribute excellent catalytic properties of Fe_3C, reducing the reaction barrier in the electrochemical process. The catalytic activity, however, is proven to be of no substantial benefit to lithium storage since Fe_3C stores 1/6 Li atoms per unit (theoretical capacity: $\sim$26 mA h g^{-1}) in a complete lithiation process.[15] Further evidence shows the absence of an observable shift in the characteristic X-ray diffraction (XRD) peaks of the Fe_3C/Fe anode during the charge and discharge processes, demonstrating its electrochemical inertia to lithium.[16] Nevertheless, extremely high capacities of Fe_3C anodes have been experimentally observed. For instance, Zhang *et al.* synthesized a graphene/Fe–Fe_3C nanocomposite with a capacity of 607 mA h g^{-1} at 1 A g^{-1}.[17] Liu *et al.* prepared nonstructural C/Fe–Fe_3C anodes possessing a considerably increased capacity of 780 mA h g^{-1} at 0.1 A g^{-1}.[18] Nevertheless, the origin of such capacity enhancements has not been fully understood to date.[15] Similar capacity enhancements have also been observed in most transition metal-based compounds (ESI,† Table S1). Theories have been proposed to trace the origin of the extra capacity: (1) Srinivasan *et al.* proposed that the grain boundaries of the metal–Li_2O phase on the Fe_2O_3 anode stores extra lithium in reduction processes;[19] (2) Zhang *et al.* reported that $CoCO_3$ converted to Li_2O and Li-intercalated Li_xC_2 (x = 0, 1, 2);[20] (3) Lu *et al.* proposed that each Mo atom additionally accommodated six Li^+ after the complete reduction of MoS_2.[21] All the aforementioned theories involve "conversion" reactions of anode materials, leading to the formation of solid electrolyte interphase (SEI) compounds (Li_2O and Li_2CO_3) and transition metals. However, Fe_3C and Fe are not involved in the conversion reactions due to their electrochemical inertness to Li. In particular, Fe is inevitably present in a Fe_3C anode due to the eutectoid transformation of both Fe and Fe_3C in the carbothermal reduction process.[22] Although metallic Fe can be removed from the carbon-coated Fe_3C/Fe nanoparticles by using HCl solutions, Fe_3C is also dissolved, which decreases the energy density of the anode.[23] Researchers believe that Fe_3C catalyzes reversible formation and decomposition of SEI, thereby giving rise to extra capacity,[16,24–26] but the specific conversion process in the SEI is rather ambiguous.

Here, we investigate the origin of the extra capacity by revealing the structural and physiochemical evolution of the SEI near a core–shell C@Fe_3C/Fe anode coupled with predesigned electrolytes of various fluorine contents. We find that the reversible conversion between esters and ethers in the SEI, as catalyzed by Fe_3C, counts mainly for the additional lithium storage. This process is enabled by C@Fe_3C with a well-tailored electron structure. The Fe atom also contributes capacity by transforming to FeF_3 active sites through LiF intermediates with a surficial haloid conversion reaction in the SEI.[27] Based on systematic *in situ* Raman and density functional theory (DFT) studies, it is verified that both organic and inorganic ingredients in the SEI undergo reversible conversion, thus giving rise to the extra capacity. Surface capacitive effects and Li^+ inter/deintercalation processes of surface carbonaceous materials are not negligible for additional capacity. The findings offer a fundamental basis towards the understanding of the electrochemical mechanism of TMCs for high-capacity battery anodes.

Results and discussion

Synthesis and characterization of core–shell C@Fe_3C/Fe

As illustrated in Fig. 1a, the crystal structure of Fe_3C features an octahedral framework. Each rhombic octahedron consists of six iron atoms, within which resides a carbon atom.[28] The covalent electrons of the interstitial carbon atoms form strong covalent bonds with the 3d electrons of iron atoms.[29] The octahedron is linked together with electron clouds between iron atoms (Fig. 1b), resulting in a conductivity that is one order of magnitude higher ($\sim 10^6$ S m^{-1}) than that of conventional carbon materials (graphite: $\sim 10^5$ S m^{-1}). Core–shell C@Fe_3C/Fe nanoparticles are synthesized with a Schlenk line and through a carbothermal reduction process (see Experimental section) (Fig. 1c). $Fe(acac)_3$ is the iron precursor, and 1-octadecene (ODE) and oleic acid serve as a carbon source, solvent and surfactant, respectively. Fe_3O_4 colloid is first synthesized through pyrolysis and then reduced by carbon to form Fe in the carbothermal process. Carbon atoms then coordinate with Fe crystals to form Fe_3C.[30] The carbothermal process finally yields core–shell C@Fe_3C/Fe.

As shown in Fig. 1d and e, scanning electron microscopy (SEM) and transmission electron microscopy (TEM) images show that Fe_3C/Fe nanoparticles are coated with carbon shells and embedded in carbon nanotubes (CNTs). The elemental mapping images demonstrate the uniform dispersion of Fe_3C in the carbon matrix (ESI,† Fig. S1). CNTs are prepared with the catalysis of Fe in the surrounding carbon matrix when the temperature is above 700 °C (Fig. 1d and e).[31] The TEM analyses in Fig. 1e and f reveal that the Fe_3C/Fe particles with an average size of $\sim$30 nm are encompassed with CNTs to form a core–shell architecture. According to the analysis of high-resolution transmission electron microscopy (HRTEM), as shown in Fig. 1g and h, lattice fringes of 0.33 nm and 0.21 nm are assigned to the (0 2 0) plane of Fe_3C and (1 1 0) plane of Fe, respectively. The selected area electron diffraction (SAED) patterns show that Fe_3C nanoparticles own a high crystallinity (the inset in Fig. 1g). The interplanar spacing of the CNTs is 0.34 nm, corresponding to the (0 0 4) lattice plane (Fig. 1g).

The formation mechanism of the robust SEI near Fe_3C is illustrated in Fig. 1i. In the initial process, the $LiPF_6$ chemically decomposes to PF_5 and LiF according to the following equation (eqn (1)):

$$LiPF_6 \rightarrow LiF + PF_5 \quad (1)$$

at the anode/electrolyte interface.[32] The strong Lewis acid (PF_5) induces the polymerization of ethylene carbonate (EC) to generate polycarbonates (Fig. 1i).[33] Then, the polycarbonate moieties in the SEI layer featuring high molecular weights serve as a binder to hold the organic and inorganic components and effectively protect the electrode surface, allowing for efficient transfer of Li^+ ions at

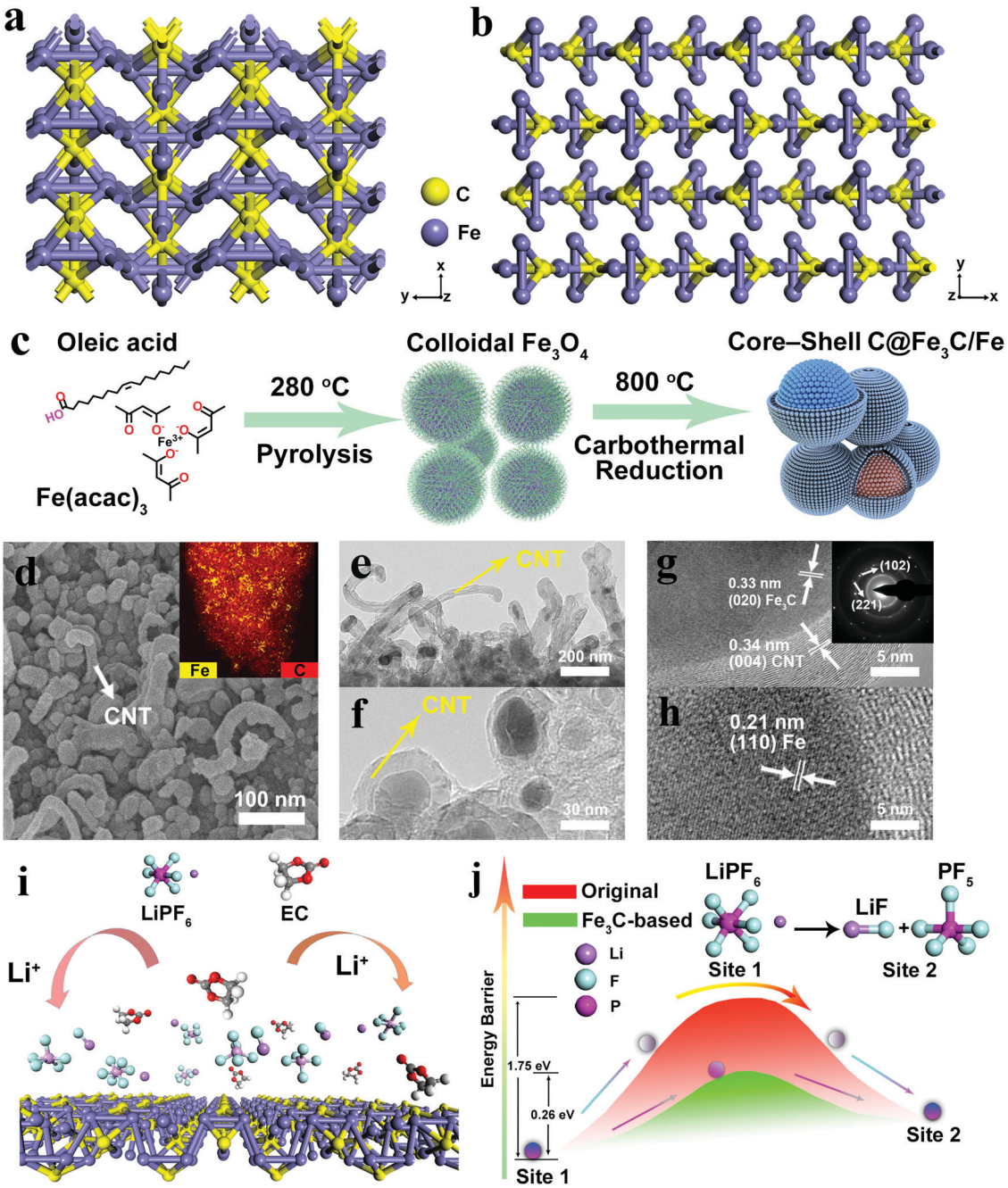

Fig. 1 Crystal/morphologic structures and characterization of core–shell C@Fe_3C/Fe particles. (a and b) The crystal structure of Fe_3C from different views. (c) Illustration of the synthetic procedure of core–shell C@Fe_3C/Fe nanoparticles (cerulean for Fe_3C, dark red for iron). (d) SEM and elemental mapping images of C@Fe_3C/Fe powders. (e and f) TEM images of C@Fe_3C/Fe powders. (g and h) HRTEM and SAED images of C@Fe_3C/Fe powders. (i) Schematics of the decomposition of $LiPF_6$ near Fe_3C. (j) The energy barriers for dissociation of $LiPF_6$ with and without Fe_3C.

the anode/electrolyte interface. DFT calculations show that the decomposition energy barrier of $LiPF_6$ on Fe_3C is 0.26 eV (Fig. 1j), which is significantly lower than that of self-dissociation in the carbonate-based electrolyte (1.75 eV), indicating the formation of a reinforced SEI layer on the carbide anode.

Physical properties of core–shell C@Fe_3C/Fe nanoparticles

The crystal structure of the synthesized C@Fe_3C/Fe is confirmed with XRD, as shown in Fig. 2, confirming orthorhombic Fe_3C (JCPDS #35-0772), cubic Fe (JCPDS #06-0696) and hexagonal CNT (JCPDS #26-1080) in C@Fe_3C/Fe. The distinguished peaks at 44.7° and 65.1° are assigned to the (1 1 0) and (2 0 0) planes of Fe. The peak at 26.6° is attributed to the (0 0 4) plane of carbon, and the prominent peaks at 37.6°, 43.7° and 54.4° are assigned to the (2 1 0), (1 0 2) and (2 3 0) planes of Fe_3C. Brunauer–Emmett–Teller (BET) gas absorptiometry determines a mesoporous structure of the core–shell nanoparticles with a high specific area of 31.1 $m^2\ g^{-1}$ (Fig. 2b and ESI,† Fig. S2), and the mesoporous structure is

further demonstrated with HRTEM (ESI,† Fig. S3b). During cell operation, Fe_3C can catalyze the electrolyte filled in the mesoporous structure of core–shell C@Fe_3C/Fe nanoparticles (ESI,† Fig. S3a). The contents of the Fe element in the carbon matrix are further confirmed with thermogravimetry analysis (TGA) in the air from 25 °C to 900 °C. As shown in Fig. 2c, from ~190 °C to 410 °C, the weight increases due to the formation of Fe_2O_3:

$$4Fe + 3O_2 \rightarrow 2Fe_2O_3 \quad (2)$$

As the temperature exceeds 410 °C, CNTs and carbon in Fe_3C are combusted to CO_2,[17] leading to a dramatic weight loss. The mass contents of Fe_3C and Fe are, therefore, calculated to be 17 wt% and 14 wt% (calculation details in the ESI†). Fig. 2d shows the Raman spectrum of C@Fe_3C/Fe. The higher intensity of the G-band (1590 cm^{-1}) as compared to that of the D-band (1310 cm^{-1}) demonstrates the high crystallinity of carbon materials, as consistent with the XRD results (Fig. 2a). The 2D peak is observed at 2700 cm^{-1}, suggesting that the sample consists of inhomogeneous multilayer graphite layers.[34] The weak peaks at 2943 cm^{-1} and 3227 cm^{-1} are attributed to the carbon overtones.

The bonding characteristics and elemental composition of C@Fe_3C/Fe nanoparticles are further confirmed with X-ray photoelectron spectroscopy (XPS). Surficial iron oxides are observed. The peaks at 710.1 eV and 723.6 eV are attributed to Fe^{2+} of Fe_3O_4, the peaks at 712.2 eV and 732.1 eV are attributed

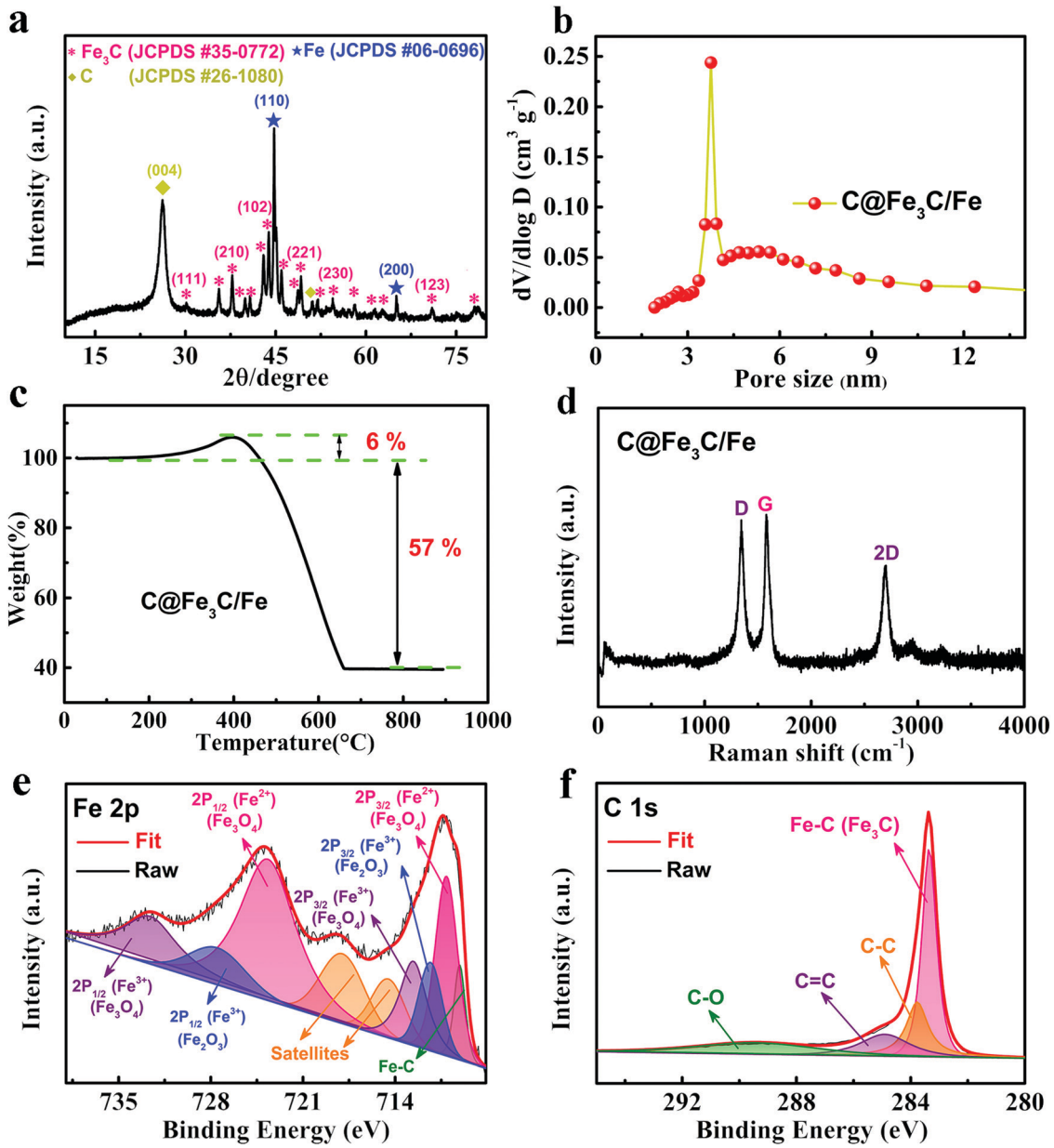

Fig. 2 Characterization of core–shell C@Fe_3C/Fe powders. (a–d) XRD patterns, pore sizes, TG curves, and Raman spectrum of C@Fe_3C/Fe powders. (e and f) High-resolution XPS spectra of Fe 2p and C 1s for C@Fe_3C/Fe.

to Fe^{3+} of Fe_3O_4, and the peaks at 711.1 eV and 727.5 eV are attributed to Fe^{3+} of Fe_2O_3, respectively.[35–37] Satellite peaks are also observed at 714.5 eV and 717.9 eV, respectively. The Fe–C peak at 708.9 eV is attributed to Fe_3C (Fig. 2e). Fig. 2f shows that the peaks at 283.7 eV, 285.1 eV and 289.3 eV for C 1s correspond to C–C, C=C and C–O bonds, respectively.[38] The dominant Fe–C peak (283.4 eV) corresponds to Fe_3C.

Core–shell C@Fe_3C/Fe anode for high-performance batteries

As shown in Fig. 3a, cyclic voltammetry (CV) is performed to analyze the electrochemical characteristics of the core–shell C@Fe_3C/Fe anode with lithium as the counter-electrode. The weak peak starting from ~1.8 V in the first lithiation process is attributed to the preliminary formation of the SEI layer with the decomposition of the electrolyte, whereas the lower peak at ~0.65 V is attributed to the further reduction of SEI. The distinct redox peaks around 0.01–0.2 V during the reduction/oxidation processes are due to the Li^+ insertion/extraction in the anodic carbon. In the reverse sweep, the broad peak at ~1.75 V corresponds to the reversible oxidization reactions of partial SEI due to the catalysis of Fe_3C.[15,17] As shown in Fig. 3b, the peaks retain the well-defined configuration even with an

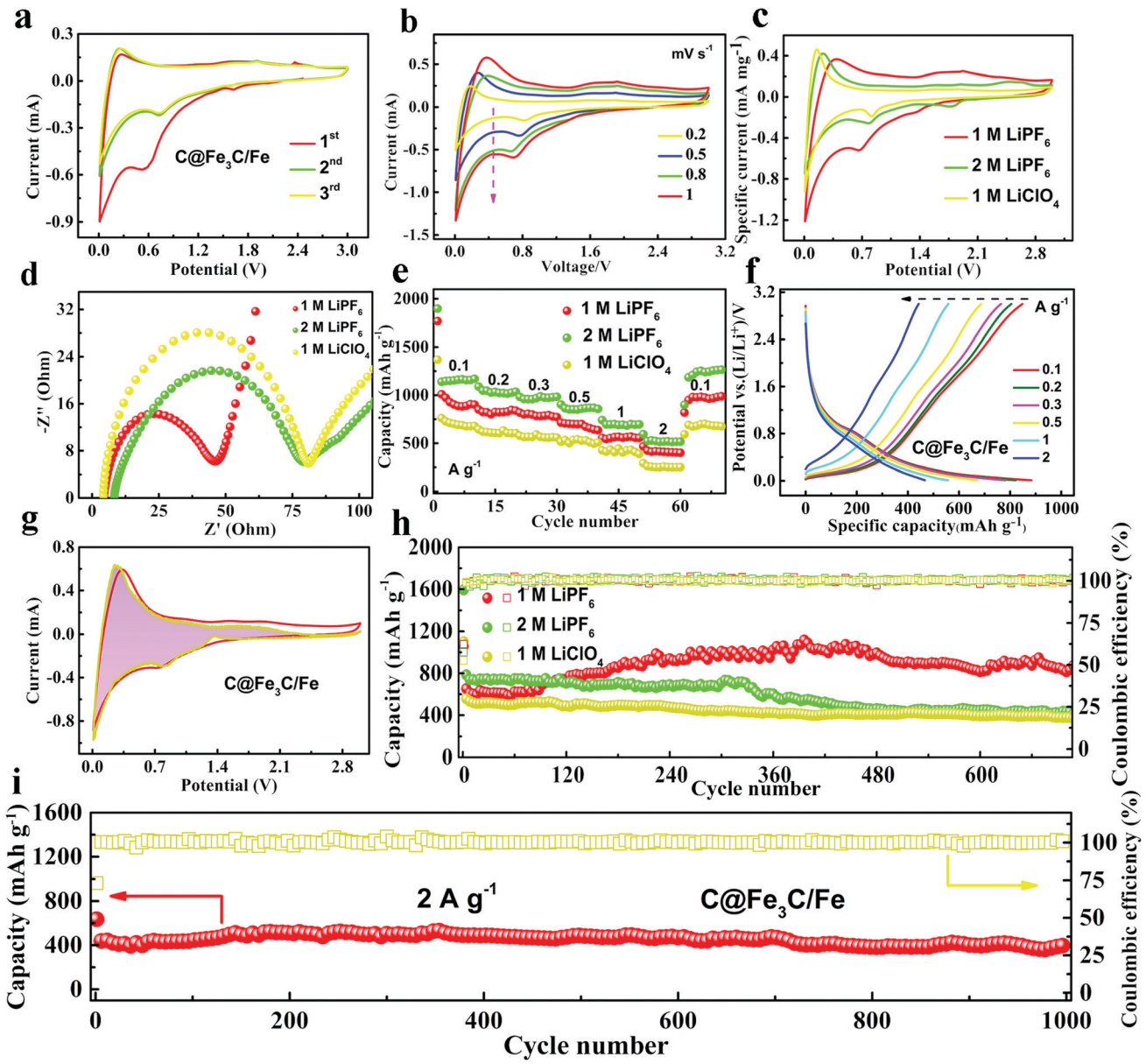

Fig. 3 Electrochemical performances of batteries with core–shell C@Fe_3C/Fe anodes. (a) Cyclic voltammograms of C@Fe_3C/Fe nanoparticles, recorded at 0.5 mV s^{-1}. (b) CV curves of C@Fe_3C/Fe nanoparticles at various scan rates. (c–e) CV curves, electrochemical impedance spectroscopies and rate performances of C@Fe_3C/Fe anodes with 1 M $LiClO_4$, 1 M $LiFP_6$ and 2 M $LiFP_6$ electrolytes. (f) Charge/discharge profiles of C@Fe_3C/Fe anodes with 1 M $LiFP_6$. (g) Current response of the C@Fe_3C/Fe anode with 1 M $LiFP_6$ at 1 mV s^{-1}. (h) Cycling performances and coulombic efficiencies of C@Fe_3C/Fe anodes with 1 M $LiClO_4$, 1 M $LiFP_6$ and 2 M $LiFP_6$ electrolytes with a current density of 1 A g^{-1}. (i) Cycling performances and coulombic efficiencies of C@Fe_3C/Fe anodes with 1 M $LiFP_6$ with a current density of 2 A g^{-1}.

increase in the scan rate from 0.2 mV to 1 mV, demonstrating the good reversibility of SEI. 1 M $LiClO_4$, 1 M $LiPF_6$ and 2 M $LiPF_6$ electrolytes are employed to investigate how the electrolyte impacts the formation of SEI (Fig. 3c). The peak intensities of 2 M $LiPF_6$ at 1.8 V (reduction process) and 2.7 V (oxidation process) are significantly enhanced compared with 1 M $LiPF_6$. However, no peaks at 1.8 V and 2.7 V are observed for 1 M $LiClO_4$, indicating that the F elements experience redox reactions in the SEI.

Electrochemical impedance spectroscopy (EIS) is employed to evaluate the interfacial resistance at the open-circuit state (Fig. 3d). The pristine cell with 1 M $LiPF_6$ possesses a smaller charge transfer resistance (R_{ct}, the semicircle diameter at the high frequency), as compared with the cell with 1 M $LiClO_4$, indicating that surface-fluoride active sites embedded in SEI lead to a reduced interfacial resistance and more pronounced electrochemical reaction kinetics of the cell. Cells after charge/discharge cycling are also tested (ESI,† Fig. S4) with various electrolytes, which demonstrates that 1 M $LiPF_6$ leads to more pronounced electrochemical reaction kinetics and lowers the cell impedance after cycling. As shown in Fig. 3e, the rate capabilities of the C@Fe_3C/Fe anode with different electrolytes are investigated. A higher concentration of fluorine in the electrolyte leads to a larger capacity. The cell with the fluorine-rich electrolyte (2 M $LiPF_6$) possesses the highest rate capacities of 1177 mA h g^{-1}, 1012 mA h g^{-1}, 954 mA h g^{-1}, 845 mA h g^{-1}, 682 mA h g^{-1} and 521 mA h g^{-1} from 0.1 A g^{-1} to 2 A g^{-1}. The discharge capacity recovers to 1195 mA h g^{-1} as the current density is reduced back to 0.1 A g^{-1} from 2 A g^{-1}. The galvanostatic charge/discharge profiles of C@Fe_3C/Fe anodes are shown in Fig. 3f. The core–shell C@Fe_3C/Fe anodes maintain the voltage plateaus even at high C rates, demonstrating the kinetically efficient Li^+ transferability at the anode/electrolyte interface and the well-retained catalytic activity of Fe_3C in the SEI.

To quantify the capacity contribution of the total capacitive and diffusion processes, C@Fe_3C/Fe anodes are investigated with CV curves at various scan rates and the results are calculated according to the following equation (eqn (3)):

$$i(V) = k_1 v + k_2 v^{\frac{1}{2}} \quad (3)$$

where $i(v)$ is the total current. $k_1 v$ and $k_2 v^{\frac{1}{2}}$ correspond to the surface and diffusion-controlled contributions, respectively.[39] The values of k_1 and k_2 at fixed potentials are determined with the following reformulated equation (eqn (4)):

$$i(V)/v^{\frac{1}{2}} = k_1 v^{\frac{1}{2}} + k_2 \quad (4)$$

As shown in Fig. 3g, the capacitive contribution accounts for 86.85% in the total charge storage at 1 mV, implying that the electrochemical reactions primarily occur at the surface. The ratio of the surface-controlled contribution at different scan rates for C@Fe_3C/Fe is illustrated in the ESI,† Fig. S5. As expected, the surface-controlled reaction kinetics gradually increases with the increase in scan rate, suggesting that a large capacitive contribution on the surface favors Li^+ storage and gives rise to a high rate capacity.[40,41]

The advantage of surficial carbon enhanced catalysis in electrochemical reactions is further elucidated with cyclic performances, as depicted in Fig. 3h. The cell with 2 M $LiPF_6$ possesses a higher initial capacity as compared with those based on 1 M $LiPF_6$ and 1 M $LiClO_4$ at the first ~100 cycles, which is consistent with the rate performances due to the high-concentration fluorides. However, large polarization and low Li^+ conductivity arising from the high-concentration lithium salt (fluoride) leads to rapid capacity decay with cycling (Fig. 3d).[42] After 700 cycles, the cell with 1 M $LiPF_6$ delivers 808 mA h g^{-1} at 1 A g^{-1}, considerably above those of 2 M $LiPF_6$ (455 mA h g^{-1}) and 1 M $LiClO_4$ (361 mA h g^{-1}). In addition, the coulombic efficiency of a C@Fe_3C/Fe anode with 1 M $LiPF_6$ rapidly reaches up to ~99% after the initial cycles. The capacity contribution of the surficial carbon during cycling is investigated by employing HCl to remove the Fe element, which is confirmed with XRD (ESI,† Fig. S3c). As shown in the ESI,† Fig. S6, surface carbon with 1 M $LiPF_6$ delivers 121 mA h g^{-1} at 1 A g^{-1}, accounting for ~14% of the total capacity of the C@Fe_3C/Fe anode. This result is consistent with the CV and current response analyses (Fig. 3g and ESI,† Fig. S5), implying that the surficial carbon contributes non-negligible capacity through the surface-controlled capacitive effect and Li^+ inter/deintercalation processes.[43,44] The catalysis of Fe_3C is further elucidated by removing metallic Fe from the composite C@Fe_3C/Fe anode. As shown in the ESI,† Fig. S7a, the XRD result shows that the peaks of Fe at 44.7° and 65.1° vanish after the HCl treatment, demonstrating that the metallic Fe has been removed. The amorphous carbon peak appears because the removal of metallic Fe increases the relative intensity of carbon. The C/Fe_3C anode possesses an increased capacity up to 500 mA h g^{-1} (ESI,† Fig. S7b), indicating that, in addition to the surface capacitive effect of surficial carbonaceous materials, Fe_3C catalyzes the reversible conversion of SEI to account for most of the additional lithium storage.

Even at 2 A g^{-1}, the cell based on the C@Fe_3C/Fe anode in 1 M $LiPF_6$ electrolyte delivers a reversible discharge capacity up to 392 mA h g^{-1} with a 99% coulombic efficiency after 1000 cycles (Fig. 3i), demonstrating the high stability of the core–shell architecture. To analyze the effects of electrolyte solvent, we add diethyl carbonate (DEC) to the 1 M $LiPF_6$ electrolyte (using ethylene carbonate + dimethyl carbonate + ethyl methyl carbonate as the solvent, denoted as EC + DMC + EMC) for electrochemical tests. As shown in the ESI,† Fig. S8a, the CV curves have the same redox peak for 1 M $LiPF_6$/EC + DMC + EMC with and without DEC, indicating that the solvents do not affect the electrochemical properties of the core–shell C@Fe_3C/Fe anode. However, the cell with 1 M $LiPF_6$/EC + DMC + EMC + DEC electrolyte exhibits increased charge transfer resistance (R_{ct}, the semicircle diameter at high frequency) and possesses a more rapid capacity decay after 400 cycles (ESI,† Fig. S8b and c).

Reaction mechanism of surface-fluoride active sites

To identify whether surficial iron oxides (Fe_2O_3 and Fe_3O_4) participate in the redox reactions, the physiochemical evolution of SEI near the core–shell C@Fe_3C/Fe anode is further identified

with XPS spectra at various potential states. No peaks of iron oxides are observed after being charged to 3 V and discharged to 0.1 V, illustrating that surficial iron oxides do not participate in the catalytic reactions. Instead, LiF and Li_2O peaks are detected (Fig. 4a–e and ESI,† Fig. S9). We propose that iron oxides are converted to Fe and Li_2O in the first lithiation process (eqn (5) and (6)).

$$Fe_2O_3 + 6Li^+ + 6e^- \rightarrow 2Fe + 3Li_2O \quad (5)$$

$$Fe_3O_4 + 8Li^+ + 8e^- \rightarrow 3Fe + 4Li_2O \quad (6)$$

The deconvolution of Fe 1s reveals characteristic FeF_3 (714.8 eV) and FeF_2 (711.3 eV) peaks, verifying the formation of surface fluoride active sites. The proportion of LiF increases from 27.6% to 40.8% as the potential decreases from 3 V to 0.1 V (Fig. 4g), indicating that inorganic LiF participates in the electrochemical reactions. DFT simulations are performed to demonstrate the strong affinity between Fe and fluorides (LiF). As shown in Fig. 4c and f, electron density difference mapping analysis shows electron accumulations between Fe(1 0 0) and LiF, suggesting the electron transfer between Fe and F as well as the formation of Fe–F bonds. We propose a conversion reaction of LiF near the Fe nanoparticles in the charge process (eqn (7)),[27] accompanied by the formation of FeF_3 active sites which store additional capacity (Fig. 4h). As shown in Fig. 4i, *in situ* Raman spectroscopy confirms FeF_3 at ~300 cm^{-1} (red bands). FeF_3 active sites experience periodic generation and consumption during charge and discharge reactions, delivering capacity as FeF_3 recovers to Fe and LiF (eqn (8)).

$$\text{Charge reaction: } Fe + 3LiF \rightarrow LiFeF_3 + 2Li^+ + 2e^- \rightarrow FeF_3 + 3Li^+ + 3e^- \quad (7)$$

$$\text{Discharge reaction: } FeF_3 + 3Li^+ + 3e^- \rightarrow LiFeF_3 + 2Li^+ + 2e^- \rightarrow Fe + 3LiF \quad (8)$$

In addition, FeF_3 can undergo a pseudocapacitive reaction and be converted to FeF_2.[45] The FeF_2 peak detected in the Fe 2p spectra is thus attributed to:[46]

$$FeF_3 + Li^+ + e^- \rightleftharpoons FeF_2 + LiF \quad (9)$$

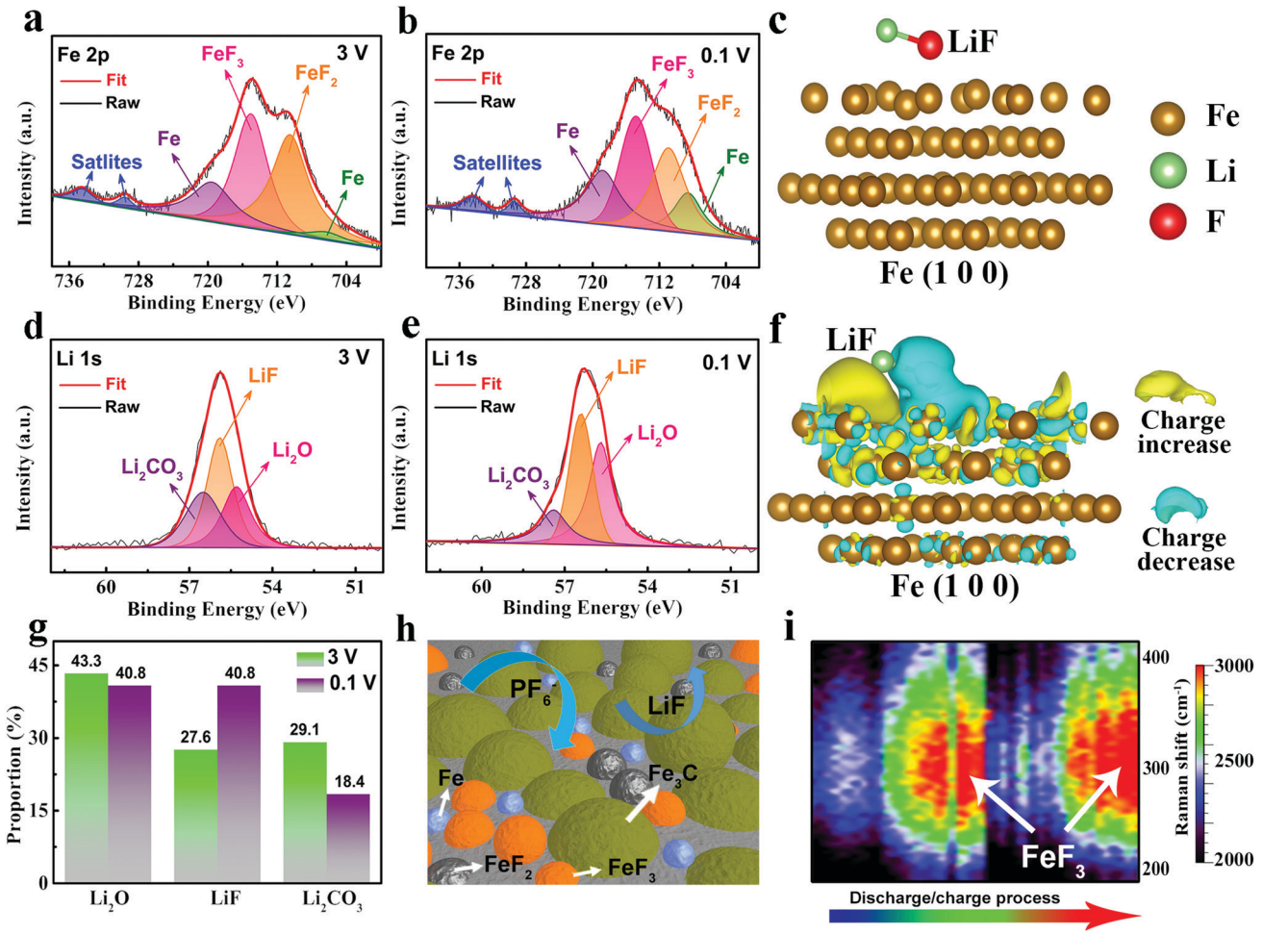

Fig. 4 DFT calculations and spectral analysis of the surficial FeF_3 active sites. (a and b) High-resolution XPS spectra of Fe 2p at the SEI on C@Fe_3C/Fe at 3 V and 0.1 V. (c) Predicted optimized configuration for interactions between Fe(1 0 0) and LiF. The isosurface level is 0.002 e $Bohr^{-1}$. (d and e) High-resolution XPS spectra of Li 1s at the SEI on C@Fe_3C/Fe at 3 V and 0.1 V. (f) Electron density difference maps for interactions between Fe(1 0 0) and LiF. (g) The variation of the inorganic composition in the SEI during the electrochemical reactions. (h) Schematics of the formation of FeF_3 active sites in the SEI layer. (i) Time-resolved Raman spectra of core–shell C@Fe_3C/Fe anodes in 1 M $LiPF_6$ electrolyte cycled at 0.2 A g^{-1}.

Based on such evidence, we believe that the reversible surficial conversion reaction of

$$Fe + 3LiF \rightleftharpoons FeF_3 + 3Li^+ + 3e^- \quad (10)$$

in the SEI contributes capacity beyond the theoretic limit for the C@Fe_3C/Fe anode. To gain further evidence, we employ commercial FeF_3 and Fe_3C materials as electrodes without adding carbon additives in electrochemical tests. As shown in the ESI,† Fig. S10a, the CV curves show that the cells based on C@Fe_3C/Fe, Fe_3C and FeF_3 electrodes all possess redox peaks in the small voltage range of 0.6–0.8 V except the anodic peak of C@Fe_3C/Fe at 0.2 V corresponding to the Li^+ extraction from the anodic carbon. This confirms that FeF_3 and Fe_3C own electrochemical properties similar to those of C@Fe_3C/Fe. The cells with commercial FeF_3 and Fe_3C deliver reversible capacities of 275 mA h g^{-1} and 103 mA h g^{-1} (ESI,† Fig. S10b), respectively. In addition, the discharge capacity of the cell based on commercial Fe_3C increases with increasing cycle number, demonstrating that the catalytic activity substantially contributes to lithium storage because Fe_3C can only store 1/6 Li atoms per unit ($\sim$26 mA h g^{-1}) in a complete lithiation process.

Evolution of SEI components under the catalysis of Fe_3C to store extra Li

To further investigate the evolution of the SEI composition associated with the capacity increment during the electrochemical reactions, XPS is employed to investigate the different redox states. As shown in Fig. 5a, hydrocarbon/carbon–carbon bonds (284.4–285.1 eV, CH_2–CH_2O), polyether carbon ($\sim$286.5 eV, CH_2O), carbonyl groups ($\sim$289.7 eV, CO_3) and polycarbonates (292.9 eV, poly(CO_3)) are observed in the C 1s spectrum at 0.1 V.[47–49] The prominent carbonyl group originates from the decomposition of carbonate solvents. The observation of polycarbonates is due to the polymerization of EC solvents induced with $LiPF_6$ decomposition, and the enriched polycarbonate moieties with high molecular weights serve as polymeric binders to integrate the SEI and intimately stick to the C@Fe_3C/Fe anode.[33] As the potential increases to 3 V, the surface organic components in the SEI layer remain unchanged but the proportion varies with the catalysis of Fe_3C (ESI,† Fig. S11). The proportion of carbonyl compounds increases to 57.2% from 42.5% with a decreasing proportion of ether-based compounds from 13.8% to 10%, which is consistent with the results from Wohlfahrt–Mehrens.[50] In addition, the variation tendency of hydrocarbon is similar to polyether, which decreases from 38% to 27.2%. However, the proportion of polycarbonate remains $\sim$5.6%, suggesting that polycarbonate stabilizes the SEI integrity in the electrochemical processes. The depth profiles of the XPS for the selected elements are illustrated in the ESI† Fig. S12. The concentrations of C and O at 0.1 V and 3 V decrease with increasing concentrations of Li and F from the outer layer to the inner layer of the SEI, indicating that organic compounds are close to the electrolyte solution and inorganic ingredients are rich in the inner SEI layer (ESI,† Fig. S12a and b). In addition, the concentrations of Li and F at 0.1 V are higher than those at 3 V, which is consistent with the electrochemical reaction mechanism of FeF_3 active sites during the formation of LiF (0.1 V) at the electrode surface (Fig. 4h). As the etching time increases, the peak of Li carbides (283.2 eV, RLi) appears with the disappearance of polycarbonates (292.9 eV, poly(CO_3)) at 0.1 V and 3 V,[33] suggesting that Li carbides are stable in the SEI during the electrochemical reactions (ESI,† Fig. S12c and d). The evolution of ethers is also confirmed with *in situ* Raman analysis, as shown in Fig. 5c. The peaks of ether bonds (800 cm^{-1} and 1050 cm^{-1}) exhibit periodic variations in the electrochemical reactions,[51] which is consistent with the XPS results.

We propose that an important aspect of the aforementioned scenario is initiated with the reduction of ester carbonates (EC and DMC) to Li-containing species (*e.g.*, CH_3OLi, $LiOCH_2CH_2OLi$, $CH_3OC(O)OCH_2CH_2OLi$) in the lithiation process near the core–shell C@Fe_3C/Fe anode, as shown in Fig. 5d. These Li-containing species in the SEI are eventually polymerized to oligomers/polymers that contain ester and ether functional groups ($LiOCH_2$-$CH_2OC(O)OCH_2CH_2OCH_2CH_2OLi$) under the catalysis of Fe_3C, which causes an increased amount of ether, decreased amount of esters and accompanying lithium storage.[51,52] Reversibly, the esters groups reconvert to ether groups through RLi and ROLi (R denotes the alkyl groups) intermediates in the delithiation processes accompanying the formation of Li_2O.[33] The unvaried polycarbonate ingredients, as a binder to hold the organic and inorganic components due to the high molecular weights, effectively protect the electrode surface (ESI,† Fig. S13a and b) and retain the integrity of the SEI with a thickness of 15 nm in the electrochemical reactions (ESI,† Fig. S13c), which is also confirmed through high angle annular dark field (HAADF) imaging (ESI,† Fig. S14a). Fe elemental mapping is performed on the cycled C@Fe_3C/Fe anode and demonstrates the growth of SEI near the iron species (ESI,† Fig. S14b). However, a higher-concentration lithium salt (2 M $LiFP_6$/EC + DMC + EMC) results in a more defective electrode surface and a thicker SEI layer (19 nm) (ESI,† Fig. S13d–f), which is consistent with the results from Li *et al.*[53] A thicker SEI possesses a lower ionic conductivity and results in a more rapid capacity decay (Fig. 3h). For 1 M $LiClO_4$/EC + DMC + EMC electrolyte, although the thickness of the SEI layer is the same as that based on 1 M $LiFP_6$/EC + DMC + EMC electrolyte, agglomerated particles occur on the post-cycle anode, which prolongs the Li^+ diffusion pathway and increases the charge transfer resistance (Fig. 3h and ESI,† Fig. S13g–i). As shown in the ESI,† Fig. S13j–l, the post-cycle anode based on 1 M $LiPF_6$/EC + DMC + EMC + DEC electrolyte possesses a rougher and thicker SEI layer (16 nm), as compared with that based on the 1 M $LiPF_6$/EC + DMC + EMC electrolyte, leading to the decrease in discharge capacity after 400 cycles (ESI,† Fig. S8b and c).

DFT calculations are performed to gain insights into the catalysis based on the core–shell C@Fe_3C/Fe architecture. We construct the structure of C@Fe_3C by combining an Fe_3C crystal and carbon sheet, and the projected 3d-orbital density of states (PDOS) of C@Fe_3C is shown in Fig. 5e (purple, dashed line). For comparison, the Fe 3d PDOS of the pristine Fe_3C is also provided in Fig. 5e (red, solid line). As compared with Fe_3C (ESI,† Fig. S15), the overlap of the projected density of states (PDOS) between the Fe_3C d-state and carbon p-state

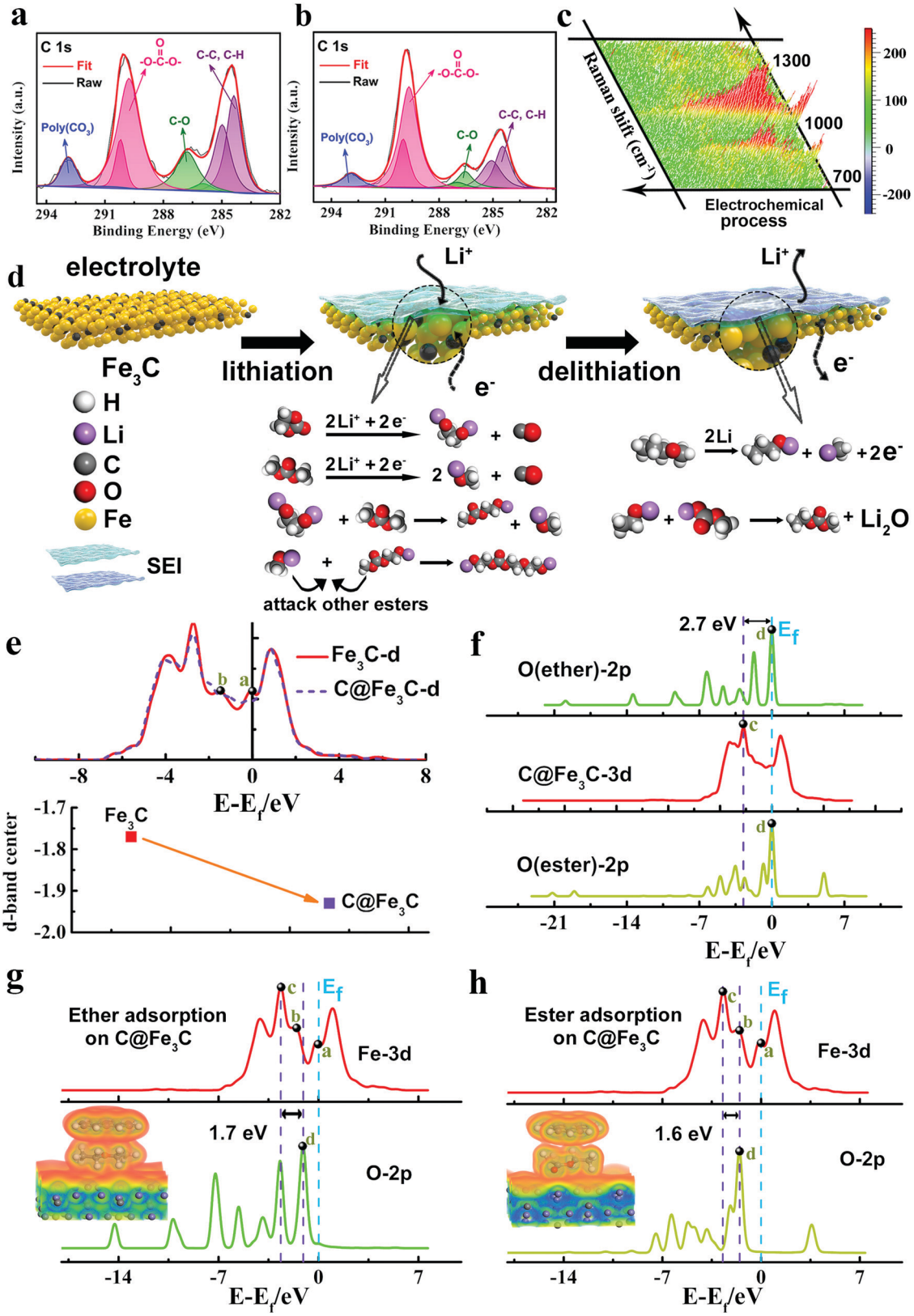

Fig. 5 DFT calculations and spectral analysis of the SEI under the catalytic effects of C@Fe_3C. (a and b) High-resolution XPS spectra of C 1s at the anode/electrolyte interface at 0.1 V and 3 V. (c) Time-resolved Raman spectra of the SEI with a 1 M $LiPF_6$ electrolyte at 0.2 A g^{-1}. (d) Schematic diagram of the reaction mechanism at the SEI layer. (e) Projected d-orbital DOS of Fe_3C with and without carbon and the corresponding d-band center. (f) The PDOS comparison of the ether, ester and Fe_3C. (g) Electron density map and PDOS comparison of ether on C@Fe_3C. (h) Electron density map and PDOS comparison of ester on C@Fe_3C.

(ESI,† Fig. S16) indicates that the Fe_3C d-orbital and the carbon p-orbital share matched energy values, demonstrating that there is robust host–guest electronic interaction between the encased Fe_3C and protective graphitic layers (ESI,† Fig. S17).[54,55] Electron density difference maps are employed to analyze the electron transfer direction within C@Fe_3C. The red and blue regions indicate a charge increase and decrease, respectively. As compared with pure carbon (ESI,† Fig. S18a), electric charges significantly increase (red region) in carbon after being incorporated with Fe_3C (ESI,† Fig. S18b), indicating electron transfer from Fe_3C to the outer layer of graphite. The electron transfer makes the carbon layer reactive to the SEI layer.[56] The delocalization of the 3d electrons broadens the d-band and, thus, lowers the d-band center of Fe_3C (Fig. 5e). The rate-determining step of catalysis is the bonding process between the adsorbate and the catalyst (C@Fe_3C) surface. The low-lying d-band center indicates that the anti-bond formed with ether/ester and C@Fe_3C is closer to the Fermi level,[57] leading to more electrons in the anti-bonds, weakening the bond between intermediates and Fe_3C, and releasing Fe_3C to accelerate the catalytic reactions.

$CH_3CH_2OCH_2CH_3$ and $CH_3C(O)OCH_2CH_3$ are taken to represent ether and ester groups, and the corresponding O 2p orbitals and C@Fe_3C 3d orbitals are shown in Fig. 5f. The Fe 3d orbital and the O 2p orbital of ether/ester have a well-matched covering range near the Fermi level (Fig. 5f), indicating the efficient electron transfer between them to accelerate the catalytic reactions. As C@Fe_3C interacts with ether and ester, the O 2p orbitals of the ether and ester and the Fe 3d orbital of C@Fe_3C are simulated and shown in Fig. 5g and h, respectively. As the ether and ester adsorb on C@Fe_3C, overlapped electron density maps for ether-C@Fe_3C (Fig. 5g) and ester-C@Fe_3C (Fig. 5h) adsorptions indicate the efficient electron transfer within ether-C@Fe_3C and ester-C@Fe_3C combinations. As compared with the pristine O 2p orbitals of ether and ester (d dots in Fig. 5f), both dominant O 2p orbital peaks of ether (d dot in Fig. 5g) and ester (d dots in Fig. 5h) shift towards lower values upon adsorption on C@Fe_3C. This narrows the energy gap between the dominant Fe 3d peak of C@Fe_3C (c dot) and the O 2p orbital of ether (d dot) from 2.7 eV to 1.7 eV (Fig. 5g), and also narrows the energy gap between the dominant Fe 3d peak of C@Fe_3C (c dot) and the O 2p orbital of the ester (d dot) from 2.7 eV to 1.6 eV (Fig. 5h). Upon adsorption, the reduced energy gaps result in stronger repulsion of the lone pair electrons between ether and C@Fe_3C and between ester and C@Fe_3C,[58] which weakens the Fe–O bonding, reduces the associated desorption barrier and facilitates the catalytic reactions of ether and ester with C@Fe_3C.

XPS results in Fig. 4a and b show that metallic Fe is present at 3 V and 1 V, suggesting that Fe embedded in the SEI is not completely converted to FeF_3 in the charge process. We fabricate Fe electrodes with commercial Fe powders to analyze the catalysis of Fe in the electrochemical reactions. Cubic Fe does not store capacity through alloying with Li because of their relatively high electronegativity difference (0.85) and unmatched valence state (+1 *vs.* +3) according to the Hume-Rothery rules.[59] Experimental results illustrate that Fe–Li alloys do not form in the battery system.[60] Additionally, the Fe–Li phase diagram fails to support the formation of Fe–Li alloys since Fe–Li alloys do not form below 1340 °C, a temperature at which Li vaporizes and Fe still remains solid.[61] However, Fe can participate in the surface conversion reaction $Fe + 3LiF \rightleftharpoons FeF_3 + 3Li$ (eqn 10) to contribute capacity. As shown in the ESI,† Fig. S19a, the charge/discharge profiles of Fe appear similar to those of Fe_3C and C@Fe_3C/Fe, indicating their similar electrochemical reactions. As the potential decreases to 0.01 V, the electrolyte is decomposed and the SEI forms on the Fe surface. Bonding processes between the adsorbate and the Fe are the rate-limiting step for catalysis. The unpaired electrons and empty orbitals in the 3d band of Fe activate the P–F bonds of $LiPF_6$ and C–O groups of ether/ester molecules, which accelerates P–F bond breaking to form LiF ($LiPF_6 \rightarrow LiF + PF_5$, eqn (1)) and enables the conversion between esters and ethers in the SEI to store capacity.[15] Nevertheless, the d-band center of Fe is −0.92 eV,[62] which is significantly higher than that of Fe_3C (−1.78 eV) (Fig. 5e), leading to poor catalysis of the conversion between esters and ethers in the SEI and the reduced formation of LiF. This, in turn, inhibits the surface reversible conversion reactions of Fe (eqn (10)) for storing extra capacity. Fig. S19b (ESI†) shows that the cell based on the Fe electrode delivers a capacity of ~28 mA h g^{-1} at 1 A g^{-1}, accounting for ~3.2% of the total capacity of the C@Fe_3C/Fe anode. Therefore, it is safe to conclude that the catalytic effect of Fe is negligible for the capacity of the C@Fe_3C/Fe anode.

Conclusions

In summary, the origin of the capacity enhancement near the high-capacity C@Fe_3C/Fe anode is revealed by directly characterizing the structural and physiochemical evolution of the SEI. Owing to the decreased d-band center of C@Fe_3C, the surficial carbon enhances the catalytic reactions that facilitate the conversion between esters and ethers at the anode/electrolyte interface and contribute capacity. A haloid conversion reaction with resultant fluoride (FeF_3) active sites in the SEI layer is demonstrated to deliver additional capacity with both experimental characterization and theoretical calculations. In addition, the surficial carbon delivers additional capacity through a surface-controlled capacitive effect and Li^+ inter/deintercalation processes. Based on the proposed Li^+-storage mechanism, the cell assembled with the C@Fe_3C/Fe anode and 1 M $LiPF_6$ electrolyte delivers a high capacity of 392 mA h g^{-1} with a 99% coulombic efficiency after 1000 cycles at 2 A g^{-1}.

Experimental section

Materials

$Fe(acac)_3$, oleic acid and ODE were supplied by Aladdin (Shanghai Aladdin Bio-Chem Technology Co., Ltd). Fe, $FeCl_3{\cdot}H_2O$, ethanol (99.7%) and *n*-hexane were purchased from Chron Chemicals (Chengdu Chron Chemicals Co., Ltd). Commercial FeF_3 and Fe_3C were supplied by Shanghai TITAN (Shanghai TITAN Technology Co., Ltd) and Bike Material (Shanghai Bike Material Technology

Co., Ltd). All the chemical reagents were analytical grade and used without further purification.

Synthesis of core–shell C@Fe_3C/Fe

$Fe(acac)_3$ was used as the iron precursor and the mixture of ODE and oleic acid was chosen as the reaction solution. Core–shell C@Fe_3C/Fe nanoparticles were prepared by dispersing 1.4 g $Fe(acac)_3$ powders into a 23 mL mixed solution of ODE : oleic acid = 15 : 8 (by volume) in a Schlenk line under vacuum. The Schlenk line was pumped for 40 minutes before Ar gas was introduced. The solution was first heated at 120 °C for 2 h and then at 280 °C for 30 minutes under magnetic stirring. After cooling to room temperature, the obtained solution was centrifuged and rinsed 4 times by using a mixture of ethanol:*n*-hexane in a volume ratio of 3 : 1, and then dried at 80 °C for 48 h in an oven. The powders were then sintered at 365 °C for 1 h in a tube furnace under the Ar atmosphere, and then the temperature was increased to 800 °C at a heating rate of 5 °C min^{-1} and kept for 2 h. Finally, the composite was treated with 1 wt% HCl for 5 minutes and rinsed with deionized water to remove the impurities. The C@Fe_3C anode was obtained by soaking the C@Fe_3C/Fe composite in 5 wt% HCl for 25 minutes. Then the solution was centrifuged and rinsed with deionized water and dried at 80 °C for 12 h. To obtain surficial carbon materials, C@Fe_3C/Fe was added into 4 M HCl and 1 M $FeCl_3{\cdot}H_2O$ solution to be stirred at 60 °C for 24 h to remove Fe. Then the solution was centrifuged and rinsed with deionized water. After drying at 80 °C for 12 h, the carbon anode materials were obtained.

Characterization

The surface morphology of C@Fe_3C/Fe nanoparticles was investigated with SEM (JSM-7100F, JEOL) operated at 5 kV. The elemental composition was identified with EDX. The lattice spacing was analyzed with HRTEM (FEI G20, USA). The crystalline structure of C@Fe_3C/Fe was characterized with XRD (D/Max 2400, Rigaku) by using Cu Kα radiation. The chemical composition and bonding characteristics were investigated with XPS (Kratos XSAM 800, Al Kα radiation (144 W, 12 mA, 12 kV)). TGA (SDT 2960, USA) with a TG analyzer was performed in the temperature range from 25 °C to 900 °C at a heating rate of 10 °C min^{-1}. The Raman spectra of the samples were examined with a 785 nm laser (Renishaw). For the post-cycle C@Fe_3C/Fe anodes, the cells were opened in an Ar-filled glove box and washed with DMC solvent to remove lithium salts and impurities. The SEI was etched through 4 kV argon ions with a sputtering rate of 0.2 nm s^{-1}.

Electrochemical measurements

The anode slurry was fabricated by mixing C@Fe_3C/Fe, acetylene black and polyvinylidene fluoride (PVDF) binder with a ratio of 8 : 1 : 1 with 2.5 mL *N*-methyl-2-pyrrolidone (NMP). The slurry was then coated on copper foil and then dried at 80 °C for 12 h. The loading of C@Fe_3C/Fe in each anode was ~1.5 mg cm^{-2} with 12 mm diameter. Fe, Fe_3C and FeF_3 electrodes were obtained using the same method without adding the carbonaceous materials. For electrochemical measurements, 2032 coin-type cells were assembled with Celgard 2325 as separator and Li foil as the counter electrode. Three types of electrolytes were used to investigate the catalysis of C@Fe_3C/Fe. For a fluorine-containing electrolyte, 1 M and 2 M $LiPF_6$ were dissolved in EC : DMC : EMC = 1 : 1 : 1 (by volume). For a fluorine-free electrolyte, the electrolyte was 1 M $LiClO_4$ in EC : DMC : EMC = 1 : 1 : 1 (by volume). To consider the effects of electrolyte solvent, 1 M $LiPF_6$ was dissolved in EC : DMC : EMC : DEC = 30 : 15 : 20 : 35 (wt%). A Neware BTS-51 instrument was employed to perform the galvanostatic charge/discharge tests at various current densities in the voltage range of 0.01–3 V (*vs.* Li^+/Li). CV and EIS characterization were analyzed with a CHI660E electrochemical workstation. CV analysis was taken at various scan rates from 0.2 mV s^{-1} to 1 mV s^{-1} within the voltage range of 0.01–3 V. EIS measurements were carried out in the frequency range from 0.10 Hz to 1.0 MHz.

In situ Raman spectroscopy

In situ Raman spectroscopy was performed through Renishaw InVia Raman microscopy with a 785 nm laser. A 2 mm hole and a 5 mm hole were punched in the centers of a separator and Li foil for the assembly of the *in situ* cell with a quartz window for Raman observations. 60 μL electrolyte was used. The cell was firstly cycled three times at 0.2 A g^{-1} within the voltage range of 0.01–3 V. Then, the laser was directly illuminated on the surface of the C@Fe_3C/Fe anode during the charge and discharge processes and the Raman signals were recorded simultaneously.

DFT calculations

Fe crystal possesses a cubic structure and a space group of *Lm*3*m* (a = 2.866 Å, b = 2.866 Å, c = 2.866 Å). Fe_3C possesses an orthorhombic structure and a space group of *Pnma* (a = 5.091 Å, b = 6.743 Å, c = 4.526 Å). Fe(1 0 0) and Fe_3C(0 0 1) crystal planes, as the stable plane,[63,64] were built. For Fe_3C, a seven-layer slab with a (2 × 2 × 1) supercell was used for surface geometry optimization within the Perdew–Burke–Ernzerhof (PBE) function of generalized gradient approximation (GGA), as implemented with the Cambridge Serial Total Energy Package (CASTEP). The top two layers of Fe_3C lattice and the representative molecules (Fe, EC, $LiPF_6$, graphite, ester and ether groups) were relaxed for the calculations. A 1 × 1 × 1 *k*-point grid and cut-off energy of 340 eV were chosen for the reciprocal space grid and the tolerance of the self-consistent field (SCF) was below 2×10^{-6}. A maximum force tolerance of 0.05 eV $Å^{-1}$, an energy tolerance of 2.0×10^{-5} eV per atom and a maximum displacement tolerance of 0.001 Å were employed for calculations. For Fe–LiF calculations, a four-layer slab with a (4 × 3 × 1) supercell of Fe crystal was used for surface geometry optimization with the GGA-PBE function. The top two layers of Fe lattice and LiF were relaxed for the calculations. The SCF value was below 2×10^{-6} eV per atom. A Monkhorst–Pack mesh *k*-points grid of 3 × 2 × 1 and a cutoff energy of 400 eV were used. An energy tolerance of 2.0×10^{-5} eV per atom, a maximum force tolerance of 0.03 eV $Å^{-1}$ and a maximum displacement tolerance of 0.001 Å were used for all calculations. The energy barrier of the decomposition of $LiFP_6$ was identified by securing the state between the reactant and the product.

Conflicts of interest

There are no conflicts to declare.

Acknowledgements

This work was supported by the Fundamental Research Funds for the Central Universities (Grant No. ZYGX2015Z003), and the Sichuan Province Science and Technology Support Program (Grant No. 2016GZ0151).

References

1 T. Liu, L. Lin, X. Bi, L. Tian, K. Yang, J. Liu, M. Li, Z. Chen, J. Lu, K. Amine, K. Xu and F. Pan, *In situ* quantification of interphasial chemistry in Li-ion battery, *Nat. Nanotechnol.*, 2019, **14**, 50.

2 X. Fan, X. Ji, F. Han, J. Yue, J. Chen, L. Chen, T. Deng, J. Jiang and C. Wang, Fluorinated solid electrolyte interphase enables highly reversible solid-state li metal battery, *Sci. Adv.*, 2018, **4**, eaau9245.

3 Q. Huang, K. Turcheniuk, X. Ren, A. Magasinski, D. Gordon, N. Bensalah and G. Yushin, Insights into the effects of electrolyte composition on the performance and stability of FeF_2 conversion-type cathodes, *Adv. Energy Mater.*, 2019, **9**, 1803323.

4 M. Armand and J.-M. Tarascon, Building better batteries, *Nature*, 2008, **451**, 652.

5 D. Chen, Z. Zhou, C. Feng, W. Lv, Z. Wei, K. H. Zhang, B. Lin, S. Wu, T. Lei, X. Guo, G. Zhu, X. Jian, J. Xiong, E. Traversa, S. Dou and W. He, An upgraded lithium ion battery based on a polymeric separator incorporated with anode active materials, *Adv. Energy Mater.*, 2019, **9**, 1803627.

6 Y. Liang, C.-Z. Zhao, H. Yuan, Y. Chen, W. Zhang, J.-Q. Huang, D. Yu, Y. Liu, M.-M. Titirici, Y.-L. Chueh, H. Yu and Q. Zhang, A review of rechargeable batteries for portable electronic devices, *InfoMat*, 2019, **1**, 6.

7 X. Fan, X. Liu, W. Hu, C. Zhong and J. Lu, Advances in the development of power supplies for the internet of everything, *InfoMat*, 2019, **1**, 130.

8 J. A. Lochala, H. Zhang, Y. Wang, O. Okolo, X. Li and J. Xiao, Practical challenges in employing graphene for lithium-ion batteries and beyond, *Small Methods*, 2017, **1**, 1700099.

9 J. Jin, Z. Wang, R. Wang, J. Wang, Z. Huang, Y. Ma, H. Li, S. H. Wei, X. Huang and J. Yan, Achieving high volumetric lithium storage capacity in compact carbon materials with controllable nitrogen doping, *Adv. Funct. Mater.*, 2019, **29**, 1807441.

10 J. Billaud, F. Bouville, T. Magrini, C. Villevieille and A. R. Studart, Magnetically aligned graphite electrodes for high-rate performance Li-ion batteries, *Nat. Energy*, 2016, **1**, 16097.

11 D. Chen, H. Tan, X. Rui, Q. Zhang, Y. Feng, H. Geng, C. Li, S. Huang and Y. Yu, Oxyvanite V_3O_5: a new intercalation-type anode for lithium-ion battery, *InfoMat*, 2019, **1**, 251.

12 L. Zhao, K. Wang, W. Wei, L. Wang and W. Han, High-performance flexible sensing devices based on polyaniline/mxene nanocomposites, *InfoMat*, 2019, **1**, 407.

13 R. Qin, Using electric current to surpass the microstructure breakup limit, *Sci. Rep.*, 2017, **7**, 41451.

14 H. Chen, X. Ma and P. K. Shen, *In situ* encapsulating FeS/Fe_3C nanoparticles into nitrogen-sulfur dual-doped graphene networks for high-rate and ultra-stable lithium storage, *J. Alloys Compd.*, 2019, **779**, 193.

15 J. Zhou, T. Qian, T. Yang, M. Wang, J. Guo and C. Yan, Nanomeshes of highly crystalline nitrogen-doped carbon encapsulated Fe/Fe_3C electrodes as ultrafast and stable anodes for Li-ion batteries, *J. Mater. Chem. A*, 2015, **3**, 15008.

16 L. Su, Z. Zhou and P. Shen, Core-shell Fe@Fe_3C/C nanocomposites as anode materials for li ion batteries, *Electrochim. Acta*, 2013, **87**, 180–185.

17 Y. Tan, K. Zhu, D. Li, F. Bai, Y. Wei and P. Zhang, N-doped graphene/Fe–Fe_3C nano-composite synthesized by a Fe-based metal organic framework and its anode performance in lithium ion batteries, *Chem. Eng. J.*, 2014, **258**, 93–100.

18 X. Zhao, D. Xia, J. Yue and S. Liu, *In situ* generated nano-Fe_3C embedded into nitrogen-doped carbon for high performance anode in lithium ion battery, *Electrochim. Acta*, 2014, **116**, 292.

19 S. Chaudhari and M. Srinivasan, 1d hollow α-Fe_2O_3 electrospun nanofibers as high performance anode material for lithium ion batteries, *J. Mater. Chem.*, 2012, **22**, 23049.

20 Z. Ding, B. Yao, J. Feng and J. Zhang, Enhanced rate performance and cycling stability of a $CoCO_3$-polypyrrole composite for lithium ion battery anodes, *J. Mater. Chem. A*, 2013, **1**, 11200.

21 L. Wang, Q. Zhang, J. Zhu, X. Duan, Z. Xu, Y. Liu, H. Yang and B. Lu, Nature of extra capacity in MoS_2 electrodes: molybdenum atoms accommodate with lithium, *Energy Storage Mater.*, 2019, **16**, 37.

22 J. Chipman, Thermodynamics and phase diagram of the Fe-C system, *Metall. Mater. Trans. B*, 1972, **3**, 55.

23 Y. Liao, K. Pan, L. Wang, Q. Pan, W. Zhou, X. Miao, B. Jiang, C. Tian, G. Tian, G. Wang and H. Fu, Facile synthesis of high-crystallinity graphitic carbon/Fe3c nanocomposites as counter electrodes for high-efficiency dye-sensitized solar cells, *ACS Appl. Mater. Interfaces*, 2013, **5**, 3663–3670.

24 W. Shen, W. Kou, Y. Liu, Y. Dai, W. Zheng, G. He, S. Wang, Y. Zhang, X. Wu, S. Fan and X. Li, Fe_3C-doped asymmetric porous carbon membrane binder-free integrated materials as high performance anodes of lithium-ion batteries, *Chem. Eng. J.*, 2019, **368**, 310–320.

25 Y.-G. Huang, X.-L. Lin, X.-H. Zhang, Q.-C. Pan, Z.-X. Yan, H.-Q. Wang, J.-J. Chen and Q.-Y. Li, Fe_3C@carbon nanocapsules/expanded graphite as anode materials for lithium ion batteries, *Electrochim. Acta*, 2015, **178**, 468–475.

26 B. Joshi, J.-G. Lee, E. Samuel, H. S. Jo, T.-G. Kim, M. T. Swihart, W. Y. Yoon and S. S. Yoon, Supersonically blown reduced graphene oxide loaded Fe–Fe_3C nanofibers for lithium ion battery anodes, *J. Alloys Compd.*, 2017, **726**, 114–120.

27 T. Zhao, L. Li, R. Chen, H. Wu, X. Zhang, S. Chen, M. Xie, F. Wu, J. Lu and K. Amine, Design of surface protective layer of LiF/FeF_3 nanoparticles in Li-rich cathode for high-capacity Li-ion batteries, *Nano Energy*, 2015, **15**, 164–176.

28 C. Jiang, B. Uberuaga and S. Srinivasan, Point defect thermodynamics and diffusion in Fe_3C: A first-principles study, *Acta Mater.*, 2008, **56**, 3236–3244.
29 Z. Lv, F. Zhang, S. Sun, Z. Wang, P. Jiang, W. Zhang and W. Fu, First-principles study on the mechanical, electronic and magnetic properties of Fe_3C, *Comput. Mater. Sci.*, 2008, **44**, 690–694.
30 Z. He, J.-L. Maurice, A. Gohier, C. S. Lee, D. Pribat and C. S. Cojocaru, Iron catalysts for the growth of carbon nanofibers: Fe, Fe_3C or both?, *Chem. Mater.*, 2011, **23**, 5379–5387.
31 L. Chen, Y. Zhang, X. Liu, L. Long, S. Wang, W. Yang and J. Jia, Strongly coupled ultrasmall-Fe_7C_3/N-doped porous carbon hybrids for highly efficient Zn-air batteries, *Chem. Commun.*, 2019, **55**, 5651–5654.
32 S. Zhang, K. Xu and T. Jow, A thermal stabilizer for $LiPF_6$-based electrolytes of Li-ion cells, *Electrochem. Solid-State Lett.*, 2002, **5**, A206–A208.
33 J. Zheng, M. H. Engelhard, D. Mei, S. Jiao, B. J. Polzin, J.-G. Zhang and W. Xu, Electrolyte additive enabled fast charging and stable cycling lithium metal batteries, *Nat. Energy*, 2017, **2**, 17012.
34 D. Su, M. Cortie and G. Wang, Fabrication of N-doped graphene-carbon nanotube hybrids from prussian blue for lithium-sulfur batteries, *Adv. Energy Mater.*, 2017, **7**, 1602014.
35 Z. Y. Wu, X. X. Xu, B. C. Hu, H. W. Liang, Y. Lin, L. F. Chen and S. H. Yu, Iron carbide nanoparticles encapsulated in mesoporous Fe-N-doped carbon nanofibers for efficient electrocatalysis, *Angew. Chem.*, 2015, **54**, 8179–8183.
36 C. Guo, J. He, X. Wu, Q. Huang, Q. Wang, X. Zhao and Q. Wang, Facile fabrication of honeycomb-like carbon network-encapsulated Fe/Fe_3C/Fe_3O_4 with enhanced Li-storage performance, *ACS Appl. Mater. Interfaces*, 2018, **10**, 35994–36001.
37 K. Liu, Z. Peng, H. Wang, Y. Ren, D. Liu, J. Li, Y. Tang and N. Zhang, Fe_3C@Fe/N doped graphene-like carbon sheets as a highly efficient catalyst in Al-air batteries, *J. Electrochem. Soc.*, 2017, **164**, F475.
38 J. Li, H. Lan, H. Liu, G. Zhang, X. An, R. Liu and J. Qu, Intercalation of nanosized Fe_3C in iron/carbon to construct multifunctional interface with reduction, catalysis, corrosion resistance, and immobilization capabilities, *ACS Appl. Mater. Interfaces*, 2019, **11**, 15709–15717.
39 Q. Liang, Y. Zheng, C. Du, Y. Luo, J. Zhang, B. Li, Y. Zong and Q. Yan, General and scalable solid-state synthesis of 2d MPS_3 (M = Fe, Co, Ni) nanosheets and tuning their Li/Na storage properties, *Small Methods*, 2017, **1**, 1700304.
40 C. An, Y. Yuan, B. Zhang, L. Tang, B. Xiao, Z. He, J. Zheng and J. Lu, Graphene wrapped $FeSe_2$ nano-microspheres with high pseudocapacitive contribution for enhanced Na-ion storage, *Adv. Energy Mater.*, 2019, **9**, 1900356.
41 J. Jiang, Y. Zhang, Y. An, L. Wu, Q. Zhu, H. Dou and X. Zhang, Engineering ultrathin mMoS_2 nanosheets anchored on N-doped carbon microspheres with pseudocapacitive properties for high-performance lithium-ion capacitors, *Small Methods*, 2019, **3**, 1900081.
42 M. F. Lagadec, R. Zahn and V. Wood, Characterization and performance evaluation of lithium-ion battery separators, *Nat. Energy*, 2018, **4**, 16.
43 B. J. Landi, M. J. Ganter, C. D. Cress, R. A. DiLeo and R. P. Raffaelle, Carbon nanotubes for lithium ion batteries, *Energy Environ. Sci.*, 2009, **2**, 638–654.
44 E. Frackowiak and F. Béguin, Electrochemical storage of energy in carbon nanotubes and nanostructured carbons, *Carbon*, 2002, **40**, 1775–1787.
45 M. A. Reddy, B. Breitung, V. S. K. Chakravadhanula, C. Wall, M. Engel, C. Kübel, A. K. Powell, H. Hahn and M. Fichtner, CF_x derived carbon-FeF_2 nanocomposites for reversible lithium storage, *Adv. Energy Mater.*, 2013, **3**, 308–313.
46 S.-W. Kim, K.-W. Nam, D.-H. Seo, J. Hong, H. Kim, H. Gwon and K. Kang, Energy storage in composites of a redox couple host and a lithium ion host, *Nano Today*, 2012, **7**, 168–173.
47 X. Han, G. Xu, Z. Zhang, X. Du, P. Han, X. Zhou, G. Cui and L. Chen, An in situ interface reinforcement strategy achieving long cycle performance of dual-ion batteries, *Adv. Energy Mater.*, 2019, **9**, 1804022.
48 D. Ensling, M. Stjerndahl, A. Nytén, T. Gustafsson and J. O. Thomas, A comparative xps surface study of Li_2FeSiO_4/C cycled with LiTFSI-and $LiPF_6$-based electrolytes, *J. Mater. Chem.*, 2009, **19**, 82–88.
49 W. Zhang, S. Zhang, L. Fan, L. Gao, X. Kong, S. Li, J. Li, X. Hong and Y. Lu, Tuning the lumo energy of an organic interphase to stabilize lithium metal batteries, *ACS Energy Lett.*, 2019, 644–650.
50 M. Pfanzelt, P. Kubiak, S. Jacke, L. Dimesso, W. Jaegermann and M. Wohlfahrt-Mehrens, Sei formation on TiO_2 rutile, *J. Electrochem. Soc.*, 2012, **159**, A809–A814.
51 D. Chen, M. A. Mahmoud, J.-H. Wang, G. H. Waller, B. Zhao, C. Qu, M. A. El-Sayed and M. Liu, Operando investigation into dynamic evolution of cathode-electrolyte interfaces in a Li-ion battery, *Nano Lett.*, 2019, **19**, 2037–2043.
52 D. Aurbach, A. Zaban, Y. Ein-Eli, I. Weissman, O. Chusid, B. Markovsky, M. Levi, E. Levi, A. Schechter and E. Granot, Recent studies on the correlation between surface chemistry, morphology, three-dimensional structures and performance of Li and Li-C intercalation anodes in several important electrolyte systems, *J. Power Sources*, 1997, **68**, 91–98.
53 B. Li, Y. Wang, H. Rong, Y. Wang, J. Liu, L. Xing, M. Xu and W. Li, A novel electrolyte with the ability to form a solid electrolyte interface on the anode and cathode of a $LiMn_2O_4$/graphite battery, *J. Mater. Chem. A*, 2013, **1**, 12954–12961.
54 Y. Hu, J. O. Jensen, W. Zhang, L. N. Cleemann, W. Xing, N. J. Bjerrum and Q. Li, Hollow spheres of iron carbide nanoparticles encased in graphitic layers as oxygen reduction catalysts, *Angew. Chem., Int. Ed.*, 2014, **53**, 3675–3679.
55 J. Liu, D. Zhu, C. Guo, A. Vasileff and S.-Z. Qiao, Design strategies toward advanced MOF-derived electrocatalysts for energy-conversion reactions, *Adv. Energy Mater.*, 2017, **7**, 1700518.
56 J. Zhu, M. Xiao, C. Liu, J. Ge, J. St-Pierre and W. Xing, Growth mechanism and active site probing of Fe_3C@N-doped carbon nanotubes/C catalysts: guidance for building

highly efficient oxygen reduction electrocatalysts, *J. Mater. Chem. A*, 2015, **3**, 21451–21459.

57 B. Hammer and J. K. Norskov, Why gold is the noblest of all the metals, *Nature*, 1995, **376**, 238–240.

58 L. Xu, H. Zhao, M. Sun, B. Huang, J. Wang, J. Xia, N. Li, D. Yin, M. Luo, F. Luo, Y. Du and C. Yan, Oxygen vacancies on layered niobic acid that weaken the catalytic conversion of polysulfides in lithium-sulfur batteries, *Angew. Chem., Int. Ed.*, 2019, **58**, 11491–11496.

59 W. Hume-Rothery, The structure of metals and alloys, *Indian J. Phys.*, 1969, **11**, 74.

60 O. Mao, R. A. Dunlap and J. R. Dahn, Mechanically alloyed Sn-Fe(-C) powders as anode materials for Li-ion batteries: I. The Sn_2Fe-C system, *J. Electrochem. Soc.*, 1999, **146**, 405–413.

61 U. Kattner and B. Burton, Phase diagrams of binary iron alloys, *Alloy Phase Diagrams*, 1993, 12–28.

62 A. Ruban, B. Hammer, P. Stoltze, H. L. Skriver and J. K. Nørskov, Surface electronic structure and reactivity of transition and noble metals, *J. Mol. Catal. A: Chem.*, 1997, **115**, 421–429.

63 L. Vitos, A. V. Ruban, H. L. Skriver and J. Kollár, The surface energy of metals, *Surf. Sci.*, 1998, **411**, 186–202.

64 X. Tian, T. Wang, Y. Yang, Y.-W. Li, J. Wang and H. Jiao, Structures and energies of Cu clusters on Fe and Fe_3C surfaces from density functional theory computation, *Phys. Chem. Chem. Phys.*, 2014, **16**, 26997–27011.